Numerical Simulation of Cavitation Around a Hydrofoil and Evaluation of a RNG κ-ε Model

Lingjiu Zhou
College of Water Conservancy and Civil Engineering,
China Agricultural University,
Beijing, China 100083
e-mail: zlj09@263.net

Zhengwei Wang
Department of Thermal Engineering,
Tsinghua University,
Beijing, China 100084
e-mail: wzw@mail.tsinghua.edu.cn

Cavitating flow around a hydrofoil was simulated using a transport equation-based model with consideration of the influence of noncondensable gases. The cavity length and the pressure distributions on the suction side can be well predicted for stable cavities using the standard renormalization-group (RNG) κ-ε turbulence model with proper noncondensable gas mass fraction. The unstable cavity shedding at lower cavitation numbers was not well predicted by the standard RNG κ-ε turbulence model. A modified RNG κ-ε turbulence model was evaluated by comparing the calculated spatial-temporal pressure distributions on the suction wall with experimental data. The results showed that the predicted cavity growth and shedding cycle and its frequency agree well with the experimental data. However, the pressure increase caused by interaction of the reentrant flow and the cavity interface is overestimated, which caused the time-averaged pressure on the front part of the hydrofoil to be overestimated. The time-averaged pressure on the rear of the hydrofoil was low because the small cavity shedding on the rear part of the cavity was not predicted. [DOI: 10.1115/1.2816009]

Introduction

Cavitation occurs in a wide variety of fluid engineering systems including pumps, water turbines, propellers, and pipes. In most cases, cavitation is an undesirable phenomenon, causing significant degradation in performance and damage as well as vibration and noises. Noticeable efforts have been made in numerical simulations of cavitating flows in recent years. Most cavitation models are based on the pseudohomogeneous flow theory proposed by Kubota et al. [1], which modeled the two phase fluid as a mixture of liquid and its vapor sharing the same velocity and pressure. Reynolds-averaged Navier-Stokes (RANS) equations were solved for the mixture to obtain the velocity, pressure, and turbulence quantities. Additional equations were deduced to solve for the vapor and the liquid volume fractions.

One of the methods used to model cavitation and condensation was to use a proper state law for the mixture. Delannoy and Kueny [2] proposed a barotropic state law that strongly links the mixture density to the static pressure, which describes the mixture density in the incompressible parts, in the pure vapor parts, and in the transition zone of the flow field. This model together with modifications of the turbulence viscosity was successfully adopted to simulate cloud cavity shedding in a Venturi-type duct [3,4]. Iga et al. [5,6] used a state law similar to the barotropic state law concept, which described the mixture density as function of pressure and vapor mass fraction. Their results also agreed with the experimental data.

Another approach is the transport equation-based model (TEM), which solves an additional transport equation for either the mass or volume fraction. A source term is used to model the mass transfer caused by evaporation and condensation. Several models have been proposed for the source term. Senocak and Shyy [7,8] compared three models to develop an interfacial dynamics-based-cavitation model and pointed out that although pressure distributions predicted by different models agreed well with each other, the predicted density distributions differed. This implies that the compressibility characteristics embodied in each cavitation model differ.

In practical cavitating flows, in most engineering equipment, the operating liquid contains a finite amount of noncondensable gases dissolved in the liquid due to leakage or aeration. Noncondensable gases not only change the initial critical cavitation pressure but also affect the flow field through volume expansion and condensation. Different methods have been used to treat the noncondensable gases. Most methods have been based on a transport equation. Some methods have assumed that the densities of the liquid, vapor, and noncondensable gas are all constant. Kunz et al. [9] used an additional transport equation for the noncondensable gas. Unlike other pressure-correction-based methods, they used a dual-time, preconditioned, implicit artificial compressibility algorithm. Yuan and Schnenn [10] used the same concept but solved the transport equations using a pressure-correction method. Singhal et al. [11] also included the effect of noncondensable gases in their "full cavitation model." They considered the noncondensable gas to have a constant mass fraction and with an ideal gas density. This assumption seemed to be more reasonable since the effect of volume change of noncondensable gas was included. The model of Singhal et al. was validated by many cases related to fixed cavities and was adopted by the commercial software FLUENT for cavitating flows.

However, the noncondensable gas mass fraction was then found to excessively affect cavity behavior in practical calculations. In addition, the standard turbulence models failed to predict the instabilities for low cavitation numbers, as was also pointed out by Delgosha et al. [3,4], who then modified the turbulent viscosity (a modified renormalization-group (RNG) κ-ε model) to simulate cloud cavity shedding in a Venturi-type duct. The barotropic state law concept was adopted in their calculations to deal with the cavitation precession. Inspired by their work, the present work combines the modified turbulent viscosity with the full cavitation model. Calculations were performed for various cavitation numbers with emphasis on the influence of noncondensable gas mass fraction and the turbulence model in the simulations. The unsteady behavior of cloud cavity shedding is analyzed and the turbulence model is evaluated based on experimental data.

Contributed by the Fluids Engineering Division of ASME for publication in the JOURNAL OF FLUIDS ENGINEERING. Manuscript received January 17, 2007; final manuscript received June 30, 2007; published online December 19, 2007. Review conducted by Steven Ceccio.

Governing Equations and Cavitation Model

The fluid was assumed to be a mixture of liquid, vapor, and noncondensable gases. The flow was assumed to be pseudohomogeneous so the multiphase fluid components were assumed to share the same velocity and pressure distributions. Therefore, only one set of Favre-averaged Navier–Stokes equations was used to describe the flow. The continuity and the momentum equations for the mixture are

$$\frac{\partial \rho}{\partial t} + \nabla \cdot (\rho \mathbf{V}) = 0 \tag{1}$$

$$\frac{\partial (\rho \mathbf{V})}{\partial t} + \nabla \cdot (\rho \mathbf{V}\mathbf{V}) = -\nabla P + \nabla \cdot \left\{ (\mu + \mu_t) \left[(\nabla \mathbf{V} + \nabla \mathbf{V}^T) - \frac{2}{3} \nabla \cdot \mathbf{V} I \right] \right\} \tag{2}$$

where P is the mixture pressure, ρ is the mixture density, and $\mathbf{V}$ is the mixture velocity vector. The laminar viscosity μ is defined as a density-weighted average of the three components. μ_t is the turbulent viscosity closed by the RNG κ-ε model [12]. The mixture density ρ is defined by

$$\frac{1}{\rho} = \frac{f_v}{\rho_v} + \frac{f_{\text{ncg}}}{\rho_{\text{ncg}}} + \frac{1 - f_v - f_{\text{ncg}}}{\rho_l} \tag{3}$$

with

$$f_v = \frac{a_v \rho_v}{\rho} \quad f_{\text{ncg}} = \frac{a_{\text{ncg}} \rho_{\text{ncg}}}{\rho} \quad f_l = \frac{a_l \rho_l}{\rho} = 1 - f_v - f_{\text{ncg}} \tag{4}$$

where f_v, f_{ncg}, f_l are the component mass fractions, ρ_v, ρ_{ncg}, ρ_l are the component densities, and a_v, a_{ncg}, a_l are the component volume fractions of the vapor, gas, and liquid components. During calculation, f_{ncg} was assumed to be a very small constant. The cavitation model used to simulate vapor generation and condensation rates is

$$\frac{\partial (a_v \rho_v)}{\partial t} + \nabla \cdot (a_v \rho_v \mathbf{V}) = \frac{\partial (\rho f_v)}{\partial t} + \nabla \cdot (\rho f_v \mathbf{V}) = -C_c \frac{\sqrt{k}}{\lambda} \rho_l \rho_l \sqrt{\frac{2 \max(p - p_v, 0)}{3 \rho_l}} f_v + C_e \frac{\sqrt{k}}{\lambda} \rho_l \rho_v \sqrt{\frac{2 \max(p_v - p, 0)}{3 \rho_l}} \times (1 - f_v - f_{\text{ncg}}) \tag{5}$$

The noncondensable gases' density was calculated using the ideal gas law:

$$\rho_{\text{ncg}} = \frac{WP}{RT} \tag{6}$$

The combined vapor and gas volume fraction $a_v + a_{\text{ncg}}$ is the final void fraction.

The model uses the recommended empirical factors $c_e = 0.02$, $c_c = 0.01$ and the surface tension coefficient $\lambda = 0.0717$ N/m.

Hydrofoil Geometry and Discretization

The effect of the noncondensable gas mass fraction and the turbulence model were assessed by modeling cavitating flow around a hydrofoil, which was experimentally studied by Leroux et al. [13]. The hydrofoil used for the simulation was a two-dimensional cambered NACA66(mod) foil with the coordinates given by Leroux et al. [13]. The relative maximum thickness was 12% at 45% from the leading edge and the relative maximum camber was 2% at 50% from the leading edge. The chord length was $C = 0.150$ m. The foil was fixed within a 1 m long and 0.192 m wide square cross test section. The angle of attack was 6 deg. The freestream velocity was 5.33 m/s. Several pressures were monitored during calculations to study the pressure oscillations caused by the cavitation. On suction side, these points were named P0, P05, P1–P9 with P0 located at $x = 0$, P05 at $x = 0.05C$, P1 at $x = 0.1C$, P2 at $x = 0.2C$, etc.

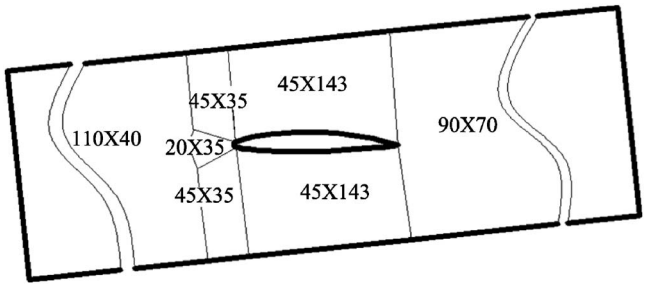

Fig. 1 Calculation domain and seven block structured grid with 27,961 nodes

The geometry was simplified to a 2D problem. The mesh was generated with seven block structured grid, as shown in Fig. 1. The mesh size was carefully selected to ensure the nondimensional normal distance from the wall (y^*) located in the log-law region since the standard wall function was adopted for near wall treatment. For a grid with 27,961 nodes, the distributions of y^* of the wall-adjacent cell's centroid were within 30–300 (see Fig. 2), so this grid was used for the following calculations.

The time-dependent equations were discretized using the control-volume technique with the SIMPLEC scheme. The second-order upwind scheme was used for the convection terms with the central difference scheme used for the diffusion terms in the momentum equations and the transport equations for κ and ε. The pressure staggering option (PRESTO) was used for the pressure interpolation. The QUICK scheme was used for the vapor mass fraction transport equation. For above grid, several time steps, 0.001 s, 0.0005 s, and 0.0001 s, were tested with $\Delta t = 0.0005$ s, found to give reasonable results with relatively short calculational times so it was used in the calculations.

Calculated Results

Simulations were performed for noncavitating flows to verify the angle of attack. The pressure distribution at an attack angle of 6 deg is plotted in Fig. 3, which shows that the calculated results agree well with the experimental data (all the experimental data in this paper are from Leroux et al. [13]).

Influence of f_{ncg} on the Simulation of Cavitating Flows With Stable Cavities. The standard RNG κ-ε turbulence model was used in calculations for cavitation numbers varying from 1.25 to 1.67 with mass fraction f_{ncg} from 1×10^{-8} to 1×10^{-6}. The influ-

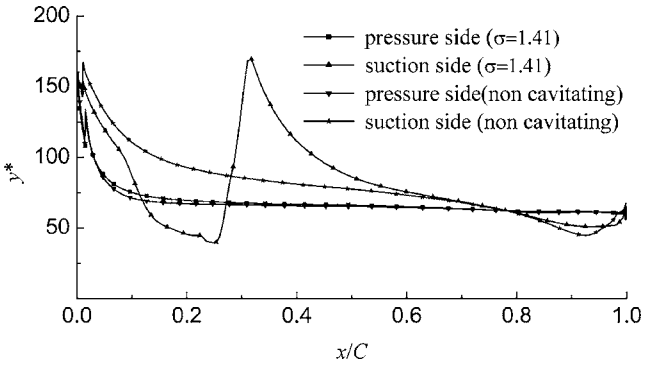

Fig. 2 Distributions of y^* of the wall-adjacent cell's centroid for noncavitating and cavitating flow

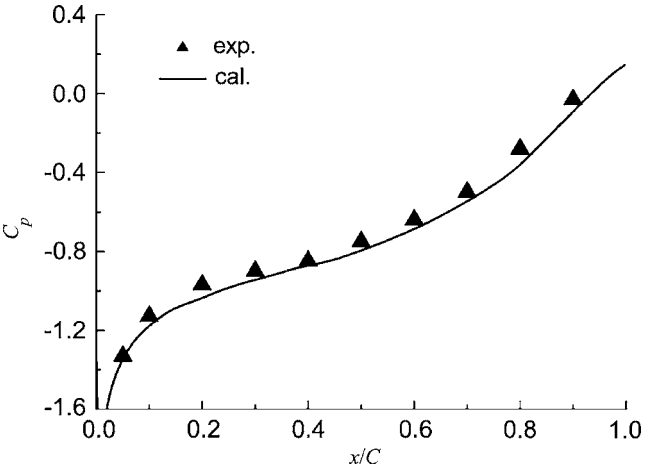

Fig. 3 Comparison of calculated result and experimental data for a noncavitating flow

ence of the mass fraction, f_{ncg}, was investigated with the results shown in Fig. 4. For a constant cavitation number, the cavity length and thickness increased with increasing noncondensable gas mass fraction up to f_{ncg} of about 1×10^{-7}. The cavity length then increased more slowly with increasing noncondensable gas mass fraction from 1×10^{-7} to 1×10^{-6} (see Fig. 4); however, the cavity thickness increased faster. Higher noncondensable gas mass fractions (1×10^{-5}) gave odd cavity shapes with the interface even reaching the upper wall of the test section, which were obviously wrong thus not presented.

The noncondensable gas mass fraction is expected to greatly influence the calculated cavity length of the pressure distribution. In the model of Singhal et al. the combined vapor and gas volume fraction a_v+a_g was used as the final void fraction. Using a_g calculated using Eqs. (4) and (6):

$$a_{\text{ncg}} = \frac{\rho f_{\text{ncg}}}{\rho_{\text{ncg}}} = \rho f_{\text{ncg}} \frac{RT}{WP} \tag{7}$$

Therefore, in this model, the noncondensable gases not only affect the mass transfer rate between the liquid and vapor (in Eq. (5), the vapor generation term) but also strongly affect the flow field as its volume increases with decreasing pressure (Eq. (7)). The calculated results show that in most of the cavity, noncondensable gas volume fraction is quite high. This also explains the fact that Eq. (5) has much lower empirical factors, c_e and c_c, than other models [7,8] that do not include noncondensable gas effects.

Figure 5 compares pressure distributions on the suction side of the profile, which shows that the cavity length and pressure distribution on the wall can be reasonably predicted if the noncondensable gas mass fraction is properly selected. For the case in Fig. 5, $f_{\text{ncg}}=6\times10^{-8}-8\times10^{-8}$ give the best results with higher noncondensable gas for lower cavitation numbers. Lower f_{ncg} (less than 6×10^{-8}) experienced some convergence difficulties.

The experimental data had more gradual pressure increases near the downstream end of the cavity than that shown in calculated results. Figure 5 shows that the calculated pressure gradient was quite steep in the closure region of the cavity with a very stable cavity. These imply that the closure region is not well predicted. Katz and Gopalan [14] observed that for sheet cavities, the cavity shapes in the closure region are highly irregular and unsteady. They indicated that cavity collapse in the closure region involves substantial increases in turbulence and momentum and displacement thickness in the boundary layer. However, the present model did not consider the interaction between the turbulence and the vapor collapse in the closure region, which might explain the lack of accuracy in the closure region.

When the predicted cavity length exceeded half the chord, the cavity became unstable, as was also observed in the experiments. The results with $f_{\text{ncg}}=8\times10^{-8}$ for $\sigma=1.25$ show that the standard RNG κ-ε model predicted an unstable cavity expanding and shrinking within $0.35C-0.6C$ with a frequency of 4.5 Hz. The typical vapor contours and velocity vectors are shown in Fig. 6. The pressure at P4 is shown in Fig. 7. There was no cavity shedding in the calculated results but the experiments revealed cloud shedding for this condition with the main frequency of the pressure oscillations of 3.625 Hz. Therefore, although the calculations predicted cavity instabilities for $\sigma=1.25$, the unsteady behavior was not correctly simulated by the standard RNG κ-ε model.

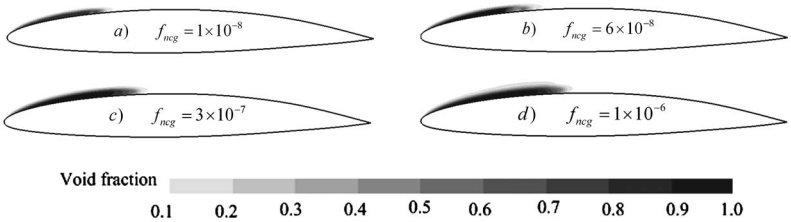

Fig. 4 Calculated cavity shape for $\sigma=1.41$ using various f_{ncg} with the standard RNG κ-ε model

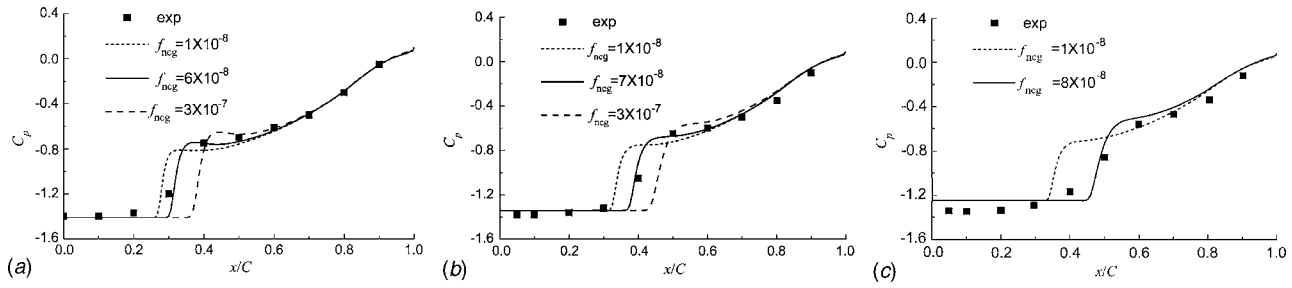

Fig. 5 Predicted pressure distribution on the suction side for various noncondensable gas mass fractions

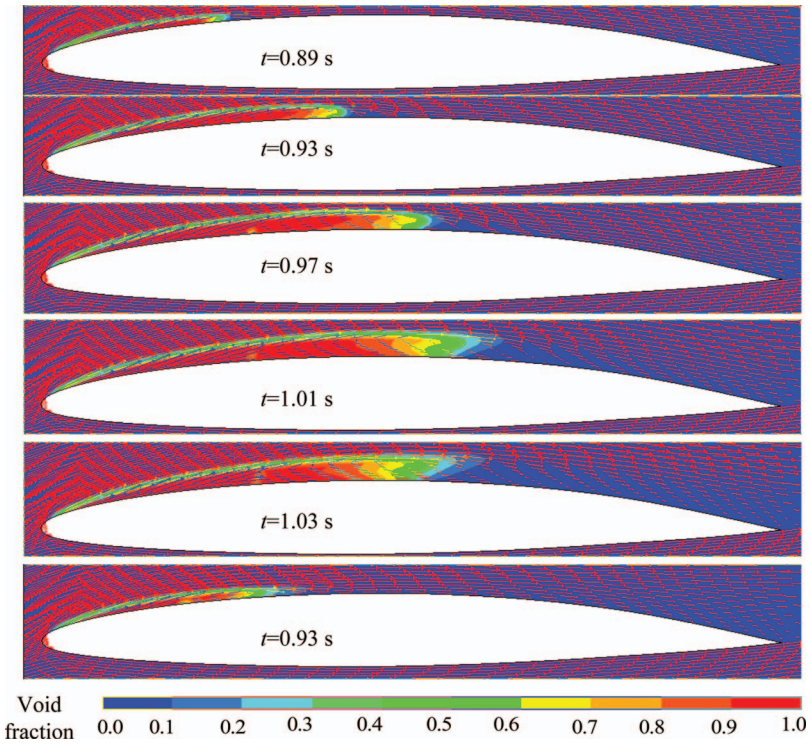

Fig. 6 Calculated void fraction contours and velocity vectors for $\sigma=1.25$ using the standard RNG κ-ε model, $f_{ncg}=8\times10^{-8}$ (to get a clear view, every four vector is displayed)

Simulations With a Modified Renormalization-Group κ-ε Model. Delgosha et al. [4] suggested a modification to the standard RNG κ-ε model, which simply reduced the mixture turbulent viscosity. In the standard RNG κ-ε model, the turbulent viscosity is defined as

$$\mu_t = \rho c_\mu \frac{k^2}{\varepsilon} \tag{8}$$

where $c_\mu=0.085$.

The modified turbulent viscosity is defined as

$$\mu_t = f(\rho) c_\mu \frac{k^2}{\varepsilon} \tag{9}$$

where

$$f(\rho) = \rho_v + (a_l)^n(\rho_l - \rho_v) \tag{10}$$

This modification was found to significantly improved simulations of the cloud shedding.

Various values of n were used in the modified RNG κ-ε model. The results showed that with $f_{ncg}=8\times10^{-8}$, $n=3-10$ gave similar results. The predicted shedding frequency was about 3.57 Hz using $n=3$ and 3.75 Hz using $n=10$, which are both close to the experimental frequency. The behavior and the development of the cavity cycle were also inspected in detail. The wall pressure fluctuations at the various points are shown in Fig. 8 for $n=3$. Only part of numerical results is shown in order to compare with the experimental results. The time axis for numerical results was panned in such a way to align the beginning of a new cycle of numerical results at 0.17 s, the initial point for the experimental cycle. Generally, the calculated pressure distributions agreed reasonably well with the experimental data and the cavity growth is predicted reasonably well. A detailed discussion is as follows.

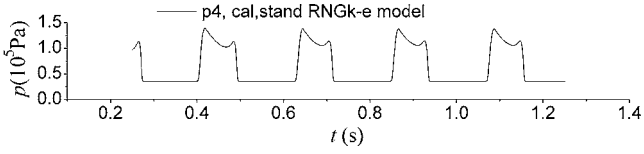

Fig. 7 Calculated pressure variations at P4 for $\sigma=1.25$ using the standard RNG κ-ε model, $f_{ncg}=8\times10^{-8}$

Discussion. The calculated cavity growth can be divided into three stages. Period A is the growth of the sheet cavity, which lasts for about 0.13 s (from 0.17 s to 0.30 s). Comparison of the spatial-temporal pressure distributions on the suction wall with experimental data shows that the sheet cavity growth period is well predicted in Period A. The sheet cavity before destabilization was about $0.7C$ long in agreement with the experimental data. Initially, the cavity has a smooth interface. Then, the reentrant flow develops at the rear of the cavity (at about $t=0.215$ s). As the cavity length exceeds 1/3 of the chord, the interface becomes wavy and the reentrant flow pushes further toward the front (see Fig. 8, $t=0.255$ s), which makes the cavity interface move upward and the cavity grow thicker. The main flow above the interface accelerates and the pressure near the rear of the cavity decreases, which causes the cavity to grow further until the cavity length reaches about $0.7C$. The pressure at points $P1-P7$ decreases to the vaporization pressure in an orderly succession.

However, some differences were noticeable. The calculated results failed to predict the small shedding on the rear part of the sheet cavity (labels a and b in Fig. 8) observed in the experiments due to the fact that the interaction between the turbulence and the vapor collapse in the closure region was not included in the model, as mentioned earlier for the stable cavity results. For the same reason, the average pressure on the rear part was estimated to be lower, as shown in Fig. 10.

Both the calculated results and the experimental data showed the pressure perturbations, which cut the cavity into two parts (see Fig. 8). Period B (from $t=0.30$ s to 0.41 s) in Fig. 9 shows that

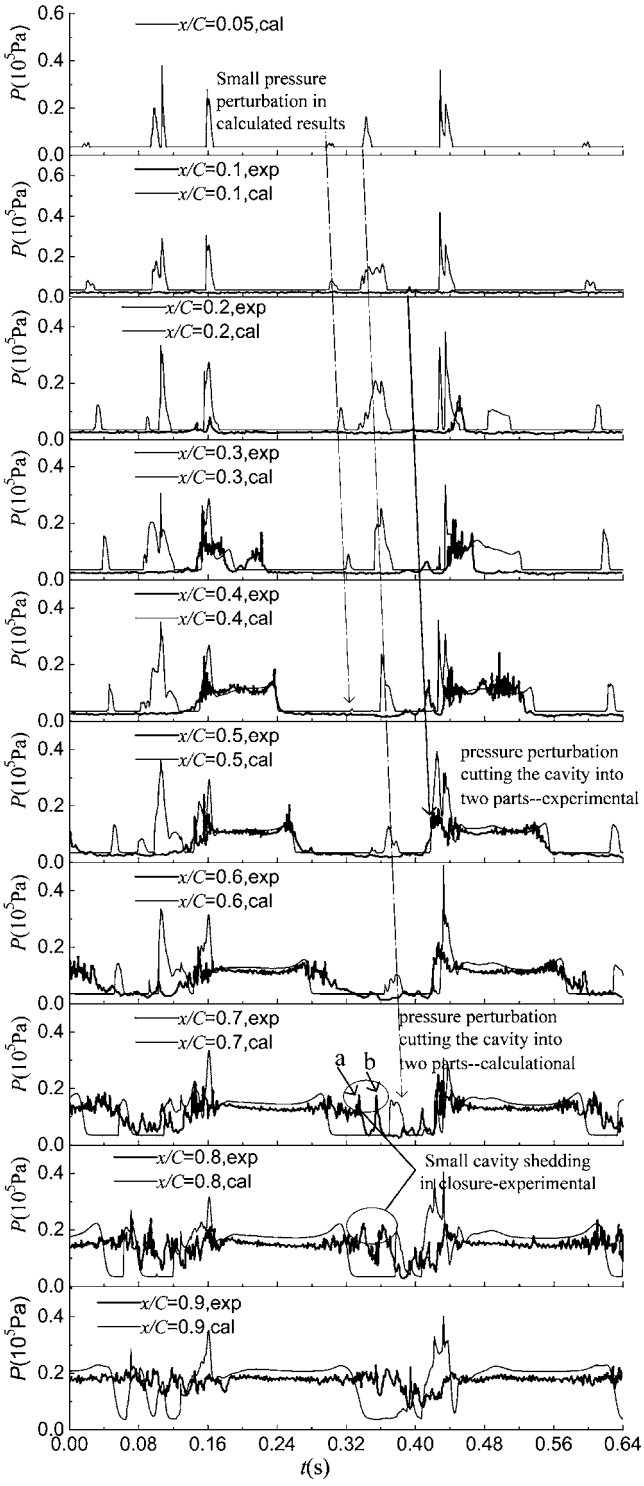

Fig. 8 Predicted pressure fluctuations during cavity growth and destabilization for $\sigma=1.25$ using the modified RNG κ-ε model, $f_{ncg}=8\times10^{-8}$

this is related to the interaction between the reversed flow and the cavity interface, which was confirmed by other researchers [15,16]. The standard RNG κ-ε model failed to predict the unstable cavity cycle, which was more accurately predicted by the modified RNG κ-ε model since the modified RNG κ-ε model reduced the turbulence viscosity within the high void fraction region. Figures 6 and 9 show that both the standard RNG κ-ε model and the modified RNG κ-ε model predicted the reversed flow in the bottom of the sheet cavity; however, the standard RNG κ-ε model did not predict that the reverse flow would reach the front of the hydrofoil. With the modified RNG κ-ε model, the reversed flow developed toward the front with negative velocities on most of the suction surface. This is consistent with the experimental results of George et al. [17] that longer partial cavities at larger attack angles showed consistently negative gas-phase velocities near the hydrofoil midchord. The reversed flow perturbed the cavity interface near the front of the hydrofoil and caused rolling up of the cavity, with this process being closely related to the vortex movement, as shown in Fig. 9. These results suggest that the interaction between the reversed flow and the cavity interface is closely related to the reduction of the turbulent viscosity. Although Delgosha et al. [4] stated that the modified model included the compressibility effect, they also noticed that the final effect of the modification was to reduce the turbulent viscosity in the vapor/liquid mixture zone. As was pointed out by Ceccio and Iyer [18] in their experiments on developed cavitation in a shear layer, the cavitation within the cores of streamwise vortices decoupled the stretching and rotation rate of these flow structures and reduced the Reynolds stresses and cross-stream velocity fluctuations. Therefore, the presence of cavitation within the shear layer may change the effective rheology of the flow. This effect may also exist in the present case with an obvious shear layer (Fig. 9). Equation (10) includes this effect in a simple way; thus, the results are improved regardless of which barotropic state law is used (the calculations of Delgosha et al. [4]) or if the full cavitation model (the present calculations) is used.

However, the modified RNG κ-ε model tends to overestimate the pressure increase caused by the interaction between the reentrant jet and the cavity interface. Figure 8 shows that the calculated pressure perturbations were much more violent on the front part of the surface and occurred a little earlier than in the experimental data. There is a small disturbance which lasts for about 0.02 s (from 0.30 s to 0.32 s) with small irregular pressure fluctuations from $0.1C$ to $0.4C$ (see Fig. 8). Then, major pressure perturbations occur caused by the shedding of the rear part of the cavity. This is initiated near the head (at $0.05C$) with a distinct pressure increase. However, in the experimental data, the major pressure perturbation was observed at approximately the middle of the cavity (at $0.4C$). In addition, the pressure perturbations lasted much longer in the calculated results than in the experimental data.

Both experimental and calculation results show that after the cavity is cut into two parts, the cavity near the head continues to grow and forms a sheet cavity while the rear part cavity moves downstream. Figure 9 shows that the moving of the rear part of the cavity is related to the rolling up of the vortex, which readjusts the velocity and pressure in the middle part of the chord. So, Fig. 8 shows a small pressure increase at each point in order, which corresponds to the growth of the front part of the cavity and the shedding of the rear part of the cavity.

The rear part of the cavity disappears in Period C. The overall pressure increase and cavity destabilization during the shedding of the rear part of cavity in Period C were predicted by the calculations. When the rear part of the cavity totally disappears into wake behind the hydrofoil, the pressure over the whole suction surface suddenly increases, which collapses sheet cavity on the front part. For some time, the whole surface is free of cavities. This period lasts for about 0.05 s (from $t=0.41$ s to 0.445 s) with another cycle then begins as the sheet cavity starts to grow again on the front part.

A shock wave is believed to occur when the rear part of the cavity collapses in the high pressure region downstream [13]. Since the present calculation assumed that the liquid phase was incompressible, the shock wave propagation could not be predicted. Figure 8 shows that the pressure increased suddenly at almost the same time (at $t=0.42$ s) at all points. The velocity vectors in Fig. 9 indicate that the shedding of the rear part of the

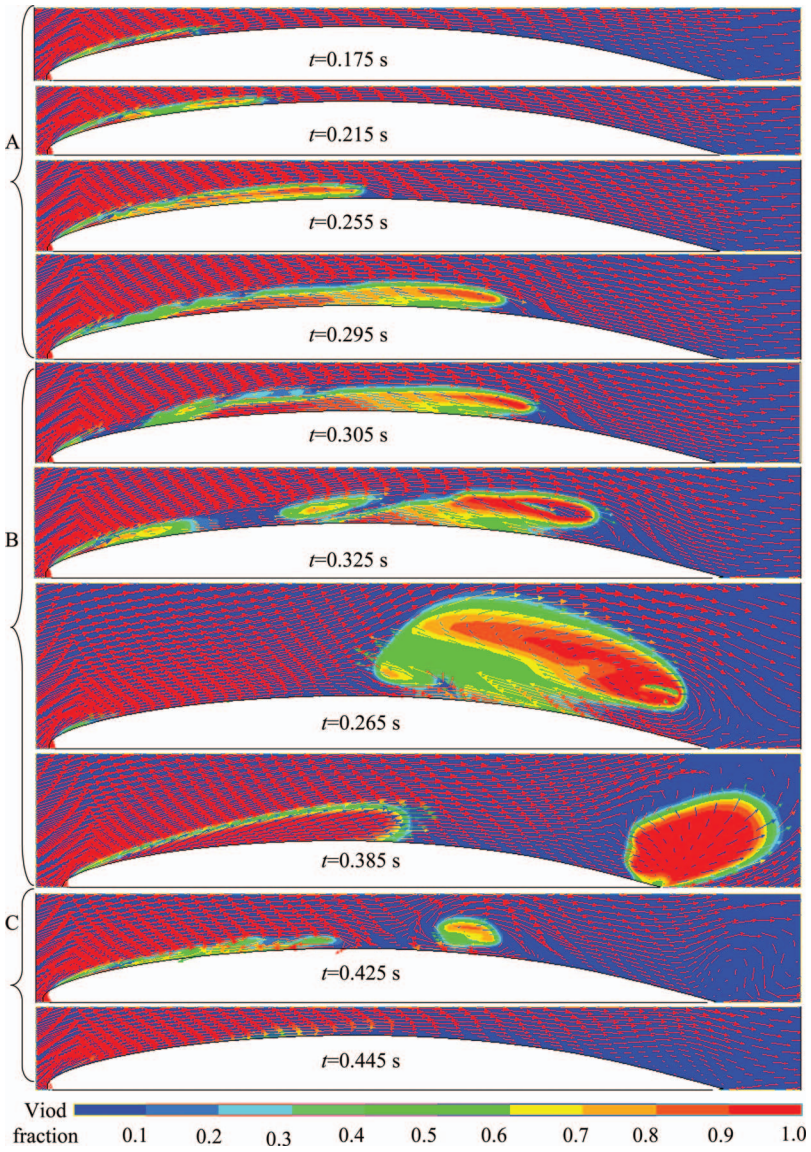

Fig. 9 Calculated void fraction contours and velocity vectors for $\sigma=1.25$ using the modified RNG κ-ε model, $f_{ncg}=8\times10^{-8}$ (to get a clear view, every four vector is displayed)

cavity is closely related to the vortex shedding. The vanishing of the cavity and the vortex reduced the blockage effects and caused the pressure increase, which quickly collapsed the remaining sheet cavity on the front part. The hydrofoil was then free of a cavitation region for a short period. The collapse of the main cavity near the back was the main reason for the pressure peak in this period. However, the predicted pressure peak was a little higher, which may due to the reason that the compressibility and bubble cloud effects were not included in the calculation: The experiments showed that the rear part cavity is bubble cloud, which can influence the fluid compressibility and wave speed and affect the collapsing behavior, while Fig. 9 shows that the calculated rear part cavity is bumpy.

Therefore, the pressure was overestimated on the front part of the hydrofoil, as shown in Fig. 10 because the pressure increase caused by interaction between the reentrant jet and the cavity interface was overestimated in Period B. The predicted pressure peak caused by the collapse of the main cavity near the back was also a little higher in Period C. The simplification from 3D problem to a 2D model can also lead to the differences of amplitude between the numerical and experimental pressure fluctuations. Therefore, much more research work is needed in the future.

Influence of n. The calculated results show that the index n had little influence on the frequency of the unstable cavity as long as n

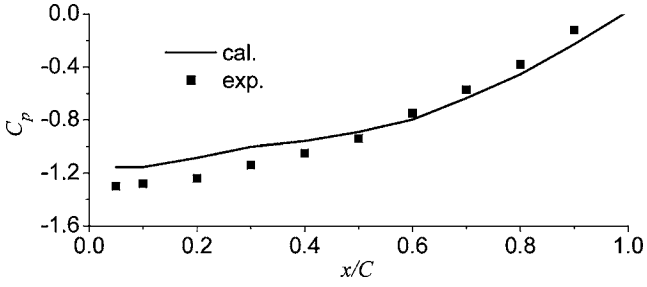

Fig. 10 Comparison of the pressure distribution on the suction surface for $\sigma=1.25$. The calculated data were obtained using the modified RNG κ-ε model, $f_{ncg}=8\times10^{-8}$.

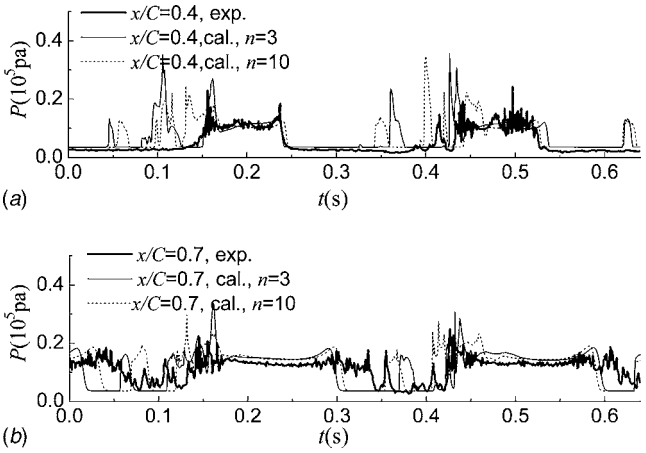

Fig. 11 Influence of parameter *n* on the predicted pressures at P4 and P7. $f_{ncg}=8\times10^{-8}$ was used for both $n=3$ and $n=10$.

was larger than 3. The cavity growth cycle for $n=10$ was also composed of three stages, the sheet cavity growth period, the pressure disturbance period with the cavity being cut into two parts, and the high pressure period after the shedding of the rear part of the cavity. The differences between the predictions for $n=10$ and $n=3$ in Fig. 11 are insignificant since the variations are similar to the variations in the experimentally measured cavity growth cycles, which were similar but not identical.

Conclusion

Cavitating flow around a hydrofoil was simulated using a TEM including noncondensable gas effects. The cavity length and the pressure distributions on the suction side were well predicted for stable cavities using the standard RNG κ-ε turbulence model with proper noncondensable gas mass fraction. However, the interaction between turbulence and the vapor collapse in the closure region was not included in the model, so the results were less accurate there.

The results showed that for lower cavitation numbers, the cavity was unstable when its length exceeded half the chord. The unstable cavity shedding at lower cavitation numbers was not well predicted by the standard RNG κ-ε turbulence model. A modified RNG κ-ε turbulence model was found to more accurately predict the shedding frequency by reducing the turbulent viscosity in the mixture region. The modified RNG κ-ε turbulence model was evaluated based on a detailed comparison of the calculated spatial-temporal pressure distributions on the suction wall with experimental data. The results showed that the cavity growth/shedding cycle characteristics and frequency agreed well with experimental data. The sheet cavity length before the rear cavity shedding was reasonably predicted. The calculated results also describe the interaction behavior between the reentrant flow and the cavity interface, which is one reason for the cavity destabilization. The sudden pressure increase along the whole wall caused by the collapse of the main cavity in the rear, which is another reason for the cavity destabilization, was also seen in the results. However, the time-averaged pressure on the front part of the hydrofoil was overestimated because the pressure increase caused by interaction between the reentrant flow and the cavity interface was overestimated. The time-averaged pressure on the rear of the hydrofoil was low because the small cavity shedding on the rear part of the cavity was not predicted.

Nomenclature

a_v, a_{ncg}, a_l = vapor, gas, and liquid volume fractions
C = hydrofoil chord (m)
C_p = pressure coefficient defined by $C_p=(p-p_r)/(0.5\rho u^2)$
f_v, f_{ncg}, f_l = vapor, gas, and liquid mass fractions
P = pressure (Pa)
P_r = pressure at reference point (Pa)
P_v = vaporization pressure (Pa), set as 3540 Pa in the present study
t = time (s)
u = freestream velocity (m/s)
$\mathbf{V}$ = velocity vector (m/s)
y^* = the nondimensional normal distance from the wall defined by $y^*=(\rho c_\mu^{1/4}k^{1/2}/\mu)y_d$, with y_d the distance to the wall
ρ = mixture density (kg/m^3)
μ = laminar viscosity ($N\,s/m^2$)
μ_t = turbulent viscosity ($N\,s/m^2$)
$\rho_v, \rho_{ncg}, \rho_l$ = vapor, gas, and liquid densities (kg/m^3)
σ = cavitation number defined by $\sigma=(p_r-p_v)/(0.5\rho u^2)$

Acknowledgment

The authors gratefully acknowledge the support from Key Technologies R&D Program for China's 11th Five-Year Plan (2006BAJ04B03).

References

[1] Kubota, A., Kato, H., and Yamaguti, H., 1992, "A New Modeling of Cavitating Flows: A Numerical Study of Unsteady Cavitation on a Hydrofoil Section," J. Fluid Mech., **240**, pp. 59–96.
[2] Delannoy, Y., and Kueny, J. L., 1990, "Two Phase Flow Approach in Unsteady Cavitation Modeling," *Cavitation and Multiphase Flow Forum*, Vol. 98, pp. 153–158.
[3] Delgosha, C. O., Reboud, J. L., and Delannoy, Y., 2003, "Numerical Simulation of the Unsteady Behaviour of Cavitating Flows," Int. J. Numer. Methods Fluids, **42**, pp. 527–548.
[4] Delgosha, C. O., Patella, F. R., and Reboud, J. L., 2003, "Evaluation of the Turbulence Model Influence on the Numerical Simulations of Unsteady Cavitation," ASME J. Fluids Eng., **125**, pp. 38–45.
[5] Iga, Y., Nohml, M., Goto, A., and Ikohagi, T., 2004, "Numerical Analysis of Cavitation Instabilities Arising in the Three-Blade Cascade," ASME J. Fluids Eng., **126**, pp. 419–429.
[6] Iga, Y., Nohml, M., Goto, A., Shin, B. R., and Ikohagi, T., 2003, "Numerical Study of Sheet Cavitation Breakoff Phenomenon on a Cascade Hydrofoil," ASME J. Fluids Eng., **125**, pp. 643–651.
[7] Senocak, I., and Shyy, W., 2004, "Interfacial Dynamics-Based Modelling of Turbulent Cavitating Flows, Part I: Model Development and Steady-State Computations," Int. J. Numer. Methods Fluids, **44**, pp. 975–995.
[8] Senocak, I., and Shyy, W., 2004, "Interfacial Dynamics-Based Modelling of Turbulent Cavitating Flows, Part II: Time-Dependent Computations," Int. J. Numer. Methods Fluids, **44**, pp. 997–1016.
[9] Kunz, R. F., Boger, D. A., Stinebring, D. R., Chyczewski, T. S., Lindau, J. W., Gibeling, H. J., Venkateswaran, S., and Govindan, T. R., 2000, "A Preconditioned Navier-Stokes Method for Two-Phase Flows With Application to Cavitation Prediction," Comput. Fluids, **29**, pp. 849–875.
[10] Yuan, W., and Schnerr, G. H., 2003, "Numerical Simulation of Two-Phase Flow in Injection Nozzles: Interaction of Cavitation and External Jet Formation," ASME J. Fluids Eng., **125**, pp. 964–969.
[11] Singhal, A. K., Athavale, M. M., Li, H. Y., and Jiang, Y., 2002, "Mathematical Basis and Validation of the Full Cavitation Model," ASME J. Fluids Eng., **124**, pp. 617–624.
[12] Yakhot, V., Orszag, S. A., Thangham, S., Gatski, T. B., and Speziale, C. G., 1992, "Development of Turbulence Models for Shear Flows by a Double Expansion Technique," Phys. Fluids A, **4**(7), pp. 1510–1520.
[13] Leroux, J. B., Astolfi, J. A., and Billard, J. Y., 2004, "An Experimental Study of Unsteady Partial Cavitation," ASME J. Fluids Eng., **126**, pp. 94–101.
[14] Katz, J., and Gopalan, S., 2000, "Flow Structure and Modeling Issues in the Closure Region of Attached Cavitation," Phys. Fluids, **12**(4), pp. 895–911.
[15] Pham, T. M., Larrarte, F., and Fruman, D. H., 1999, "Investigation of Unsteady Sheet Cavitation and Cloud Cavitation Mechanisms," ASME J. Fluids Eng., **121**, pp. 289–296.
[16] Kubota, S., Kato, H., Yamaguchi, H., and Meada, M., 1987, "Unsteady Structure Measurement of Cloud Cavitation on a Foil Section Using Conditional Sampling Technique," *International Symposium on Cavitation Research Facilities and Techniques*, Boston, pp. 161–168.
[17] George, D. L., Iyer, C. O., and Ceccio, S. L., 2000, "Measurement of the Bubbly Flow Beneath Partial Attached Cavities Using Electrical Impedance Probes," ASME J. Fluids Eng., **122**, pp. 151–155.
[18] Ceccio, S. L., and Iyer, C. O., 2002, "The Influence of Developed Cavitation on the Flow of a Turbulent Shear Layer," Phys. Fluids, **14**(10), pp. 3414–3431.